Fast Label-Free Nanoscale Composition Mapping of Eukaryotic Cells Via Scanning Dielectric Force Volume Microscopy and Machine Learning

Martí Checa, Ruben Millan-Solsona, Adrianna Glinkowska Mares, Silvia Pujals, and Gabriel Gomila*

Mapping the biochemical composition of eukaryotic cells without the use of exogenous labels is a long-sought objective in cell biology. Recently, it has been shown that composition maps on dry single bacterial cells with nanoscale spatial resolution can be inferred from quantitative nanoscale dielectric constant maps obtained with the scanning dielectric microscope. Here, it is shown that this approach can also be applied to the much more challenging case of fixed and dry eukaryotic cells, which are highly heterogeneous and show micrometric topographic variations. More importantly, it is demonstrated that the main bottleneck of the technique (the long computation times required to extract the nanoscale dielectric constant maps) can be shortcut by using supervised neural networks, decreasing them from weeks to seconds in a wokstation computer. This easy-to-use data-driven approach opens the door for in situ and on-the-fly label free nanoscale composition mapping of eukaryotic cells with scanning dielectric microscopy.

1. Introduction

The current gold standard technique to assess the local biochemical composition of eukaryotic cells is fluorescence optical micros-

copy. By means of this technique, the spatial distribution of the biochemical composition of eukaryotic cells can be obtained from the micro- to the nanoscale.[1–4] Nevertheless, fluorescence microscopy is invariably linked to the use of exogenous fluorescence probes, which can be complex to incorporate (e.g., in vivo applications), not desirable (e.g., toxicity assays) or may perturb the local properties of the cell under study. To overcome this limitation, label-free optical microscopy techniques have been also developed, with a considerable boost experienced in recent years with the incorporation of multiphonon and multiharmonic optics.[5,6] Examples include two-phonon optical microscopy to detect autofluorescence in cellular components,[7] second and third-harmonic generation methods[8] to detect fibrillar and lipid structures, Raman microscopy to detect specific chemical bonds,[9] including coherent antistokes Raman scattering for improved performance,[10] or digital holographic microscopy with quantitative refractive index mapping.[11,12]

Nonoptical label-free biochemical composition mapping methods are also possible, by probing, for instance, the local (complex) permittivity of eukaryotic cells.[13,14] Composition maps can be obtained by relating the local permittivity values measured in a cell to the permittivity of the pure biochemical components such as lipids, proteins, and nucleic acids.[15] This approach has been implemented for small-scale systems showing relatively simple geometries, like nanoparticles,[16] bacterial cells,[17,18,19] bacterial endospores,[20] virus particles,[16] protein macromolecular structures like virus tails and capsids[21] or bacterial flagella.[22] But for the case of eukaryotic cells not much progress has been reported to date due to the highly nonplanar and heterogeneous nature of the cells, which complicates the quantitative analysis of the experimental data to extract the nanoscale permittivity maps. Therefore, despite several works have reported nanoscale dielectric images of eukaryotic cells[13,23–28] only in few cases quantitative permittivity (or dielectric constant) maps have been provided.[25,26] But in these latter cases, the dielectric constant maps were obtained by making use of oversimplified theoretical cell models that gave rise to nonrealistic values for the local dielectric constants, and hence, could not be used for nanoscale composition mapping.

To overcome this drawback, we developed recently scanning dielectric force volume microscopy (SDFVM).[19] SDFVM

Dr. M. Checa,[+] R. Millan-Solsona, Prof. G. Gomila
Nanoscale Bioelectrical Characterization Group
Institute for Bioengineering of Catalonia (IBEC)
The Barcelona Institute of Science and Technology (BIST)
Carrer Baldiri i Reixac 11-15, Barcelona 08028, Spain
E-mail: ggomila@ibecbarcelona.eu
R. Millan-Solsona, Dr. S. Pujals, Prof. G. Gomila
Departament d'Enginyeria Electrònica i Biomèdica
Universitat de Barcelona
Carrer Martí i Franquès 1, Barcelona 08028, Spain
A. G. Mares, Dr. S. Pujals
Nanoscopy for Nanomedicine Group
Institute for Bioengineering of Catalonia (IBEC)
The Barcelona Institute of Science and Technology (BIST)
Carrer Baldiri i Reixac 11–15, Barcelona 08028, Spain

The ORCID identification number(s) for the author(s) of this article can be found under https://doi.org/10.1002/smtd.202100279.
[+]Present Address: ICN2-Institut Català de Nanociència i Nanotecnologia (CERCA-BIST-CSIC), Campus Universitat Autònoma de Barcelona, Bellaterra, Barcelona 08193, Spain

overcomes the limitations of existing nanoscale dielectric imaging methods concerning both data acquisition and quantitative theoretical analysis for its application to highly heterogeneous and nonplanar systems. SDFVM combines the acquisition of local electric force approach curves at each pixel of the image with its quantitative analysis by using finite element numerical calculations applied to realistic tip-sample geometrical models extracted directly from the measured sample topography.[19] The dielectric constant maps obtained in this way are fully realistic independently of the complexity of the sample topography, and hence adequate for its use for nanoscale composition mapping in cells, as it has been demonstrated for the case of bacterial cells.[19] Nevertheless, the main bottleneck of such an approach is the complex and time-consuming quantification procedure to extract the dielectric constant maps by means of finite element numerical calculations, which can take even weeks in large scale samples like eukaryotic cells.

In this work, we overcome the limitations of SDFVM applied to eukaryotic cells for nanoscale and label-free composition mapping. We first demonstrate that SDFVM, as developed earlier, can provide realistic nanoscale dielectric constant and composition maps of dry eukaryotic cells, despite their inherent complex nature. On the large scale, we show that the dielectric constant maps obtained are consistent with the biochemical composition of the cells. On the small scale, they enable identifying the composition of nanoscale biostructures present in the cells. We then demonstrate that the quantitative analysis of the experimental data can be implemented also through supervised learning algorithms using neural networks. We show that this approach reduces drastically the computation time as compared with the use of finite element numerical calculations (from months to seconds in a workstation computer), preserving the accuracy in the extracted dielectric constant maps. Both results together, open the possibility for on-the-fly label-free nanoscale dielectric and composition mapping of eukaryotic cells with scanning dielectric microscopy.

2. Results

SDFVM[19] is a scanning dielectric microscopy method[16,29–32] based on the acquisition of electric force–distance curves (normal deflection and 2ω-oscillation amplitude) at each pixel of a sample by using a fast force volume imaging scheme,[33] followed by its quantitative analysis employing theoretical tip-sample models with realistic geometries, usually solved using finite element numerical calculations.[16,17–20,22,29–32] In the case of simple samples, the geometrical models consist of geometrical figures such as spheres,[16] ellipsoids,[17,18] cylinders,[22] etc. However, for samples with complex geometries, like eukaryotic cells, this approach is no longer possible and the geometrical model needs to be built directly from the measured cell topography,[19] and then solved by using finite element numerical calculations. This fact, together with the large number of pixels per image to be processed, implies a huge computational effort, which can take even months in a workstation computer. Here, we have applied this procedure to show that SDFVM can, indeed, provide dielectric constant maps of dry eukaryotic cells consistent with their biochemical composition. Later on, we

show that an alternative procedure based on the use of neural networks can also be applied in the quantitative analysis of the data, which drastically reduces the computing time to just a small fraction of the time required to compute the dielectric constant map by using finite element numerical calculations. A schematic representation of the SDFVM method, including both possible quantitative analysis approaches, is shown in **Figure 1** (for further details see[19] and the Experimental Section).

As test sample, we consider fixed HeLa cells seeded on top of a gold-coated silicon substrate in dry air environment (see the Experimental Section). **Figure 2**a shows an optical microscopy image taken during the acquisition of the SDFVM data of one of the samples analyzed. Figure 2b,c shows the calibrated vertical Deflection [D(X,Y;Z)] and Capacitance Gradient [dC/dz (X,Y;Z)] data cubes built up from the ensemble of normal deflection and 2ω-oscillation amplitude electric force–distance curves acquired at each pixel of the image (see[19] for further details and Video S1, Supporting Information). Figure 2d shows the topographic image of the two HeLa cells located within the yellow rectangle in Figure 2a. The topographic image has been generated from the Deflection data cube in Figure 2b. Figure 2e shows the derivative of the topographic image (sometimes referred to as error or amplitude image), which better highlights the edges of the different cell structures. The maximum height of the cells is ≈1 µm, significantly smaller than for living cells due to the liquid loss during the drying and fixation process, which nevertheless is expected to preserve the structure and composition of the cell. In addition to the cell bodies, some cell membrane nanoelongations joining the two cells and some nanostructures in the cell bodies are also observed. On the cell nucleus, we observe the presence of some protuberances, which probably correspond to cell nucleoli.[34]

Figure 2f shows a lift-mode capacitance gradient, dC/dz, image obtained from the Capacitance gradient data cube in Figure 2c for a tip-sample distance $Z_{lift} = 50$ nm. This image shows a high contrast between different cell regions, which is mainly due to the presence of strong topographic crosstalk effects, as we discussed elsewhere.[35] We show it here for completeness since lift-mode is one of the most common electric force microscopy imaging modes.

Figure 2g–i shows three constant height dC/dz images obtained also from the Capacitance gradient data cube in Figure 2c at tip-substrate distances $Z_{CH} = 130$, 280, and 1080 nm, respectively. These images are free from topographic crosstalk effects and report the actual variations of the local polarization of the cell. However, the local polarization of a cell depends on the local geometrical features of the cell (e.g., thickness and radius of curvature) and tip-sample distance, and hence the constant height dC/dz images do not constitute nanoscale dielectric constant maps either. Further dC/dz images can be generated from the SDFVM data sets, including images along the XZ and YZ planes (see Supporting Information S1) but in none of the cases the dielectric images obtained from the experimental data-sets directly represent dielectric constant maps.

To build the dielectric constant maps, a quantitative theoretical analysis based on a realistic tip-sample geometrical model is necessary as we mentioned above. To reduce the computational time, instead of building a global tip-cell geometrical model,
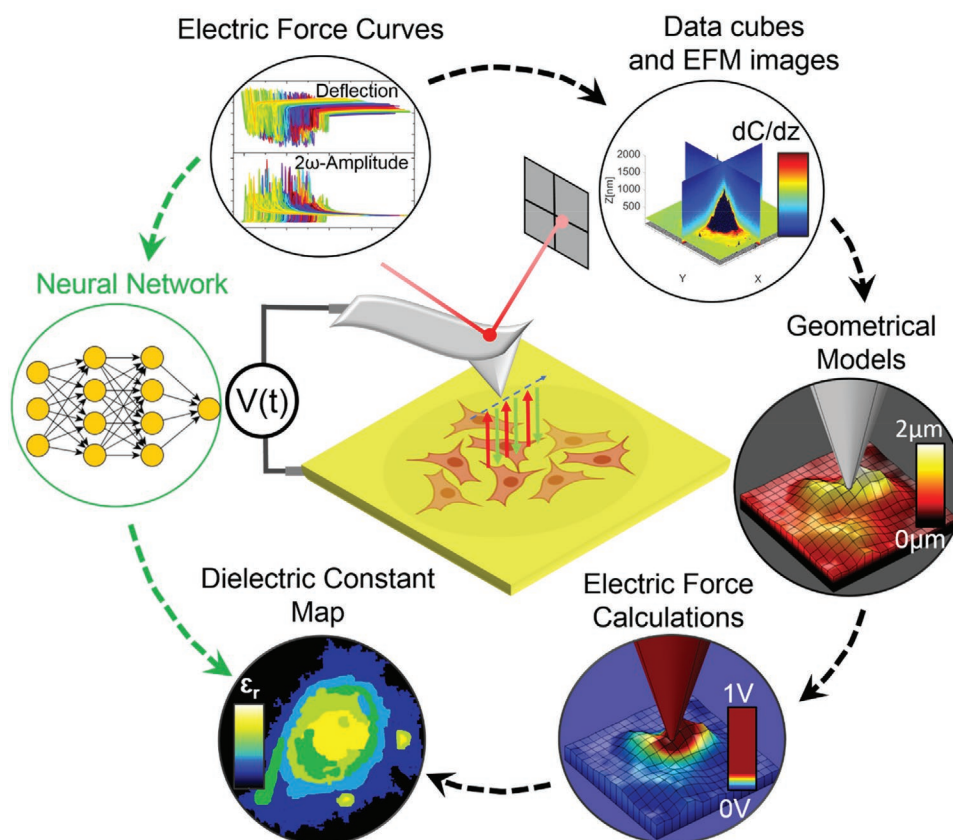
ADVANCED
SCIENCE NEWS
www.advancedsciencenews.com

small
methods
www.small-methods.com

Figure 1. Schematic representation of Scanning Dielectric Force Volume Microscopy applied to the dielectric constant mapping of eukaryotic cells. Deflection and 2ω-oscillation amplitude electric force-distance curves are acquired at each pixel of the image by using a fast force volume imaging scheme. Deflection and capacitance gradient data cubes are generated from the acquired data from where topographic and electric force microscopy images are obtained, respectively. From the topographic images, local geometrical models are built and used to compute numerically theoretical electric force curves. Quantitative dielectric constant maps are obtained by fitting the theoretical electric force curves to the experimental ones at each pixel, with the local dielectric constant as single fitting parameter. A drastic reduction of the computational effort required to implement this approach can be achieved by using supervised learning, such as neural networks.

we build local tip-cell geometrical models that include only a region of the cell around the pixel of interest.[19] An example of a local geometrical model corresponding to the topography of the dashed red square area highlighted in Figure 2k is shown in Figure 2j, with a calculated electrical potential overlaid on it. The local geometrical model includes 9×9 pixels around the pixel of interest, which ensures that local cell geometrical effects on the local polarization are correctly accounted for. At every pixel a different local cell geometrical model is built following the topographic image (see[19] and Video S2, Supporting Information).

For the tip we used the same model as in previous SDM works[16,31,32,36] and which consists of a cone ended with a tangent sphere and caped with a disc cantilever. The dimensions of the tip are calibrated using a set of SDFVM approach curves measured on a bare part of the metallic substrate[16,29] (white dashed square region in Figure 2d) giving $R = 235 \pm 14$ nm by assuming a fixed half cone angle $\theta = 20°$. The error is the standard deviation of the values corresponding to the $N = 1634$ curves analyzed (see the Supporting Information S2).

Figure 2k shows the dielectric constant map for the HeLa cells in Figure 2d obtained by following this procedure. The

spatial distribution of the dielectric constants is highly heterogeneous, as expected for a system like a eukaryotic cell. We first note that all the relative dielectric constant values satisfy $\varepsilon_{cell} < 8$. This result is in agreement with the fact that, on dry cells, the largest expected dielectric constant corresponds to nucleic acids for which $\varepsilon_{DNA} \approx 8$,[16,21] while for lipids one has $\varepsilon_{lip} \approx 2$,[30,37] and for proteins, $\varepsilon_{prot} \approx 3–4$.[22,37] This result is a first indication that topographic effects are correctly accounted for in the dielectric constant mapping procedure despite the complex cell topography. If topographic effects were not correctly accounted for, e.g., by using analytic or simple thin film tip-cell models, the extracted dielectric constants would be less realistic, as we show explicitly in the Supporting Information S3.

On the large scale, and according to the dielectric constant values displayed in Figure 2k, three regions can be identified in the HeLa cells, namely, a region with low dielectric constant values $\varepsilon_1 \approx 2$ (blue color in Figure 2k), another with intermediate values $\varepsilon_2 \approx 3–4$ (green color) and, finally, one with high values $\varepsilon_3 \approx 5–6$ (yellow color) (see also pixel histogram analysis in Figure 2l). The cell region with the low dielectric constant ($\varepsilon_1 \approx 2$) corresponds to the thinnest and more extended part of the cell ($\approx$40 nm thick), which conforms the cell membrane,
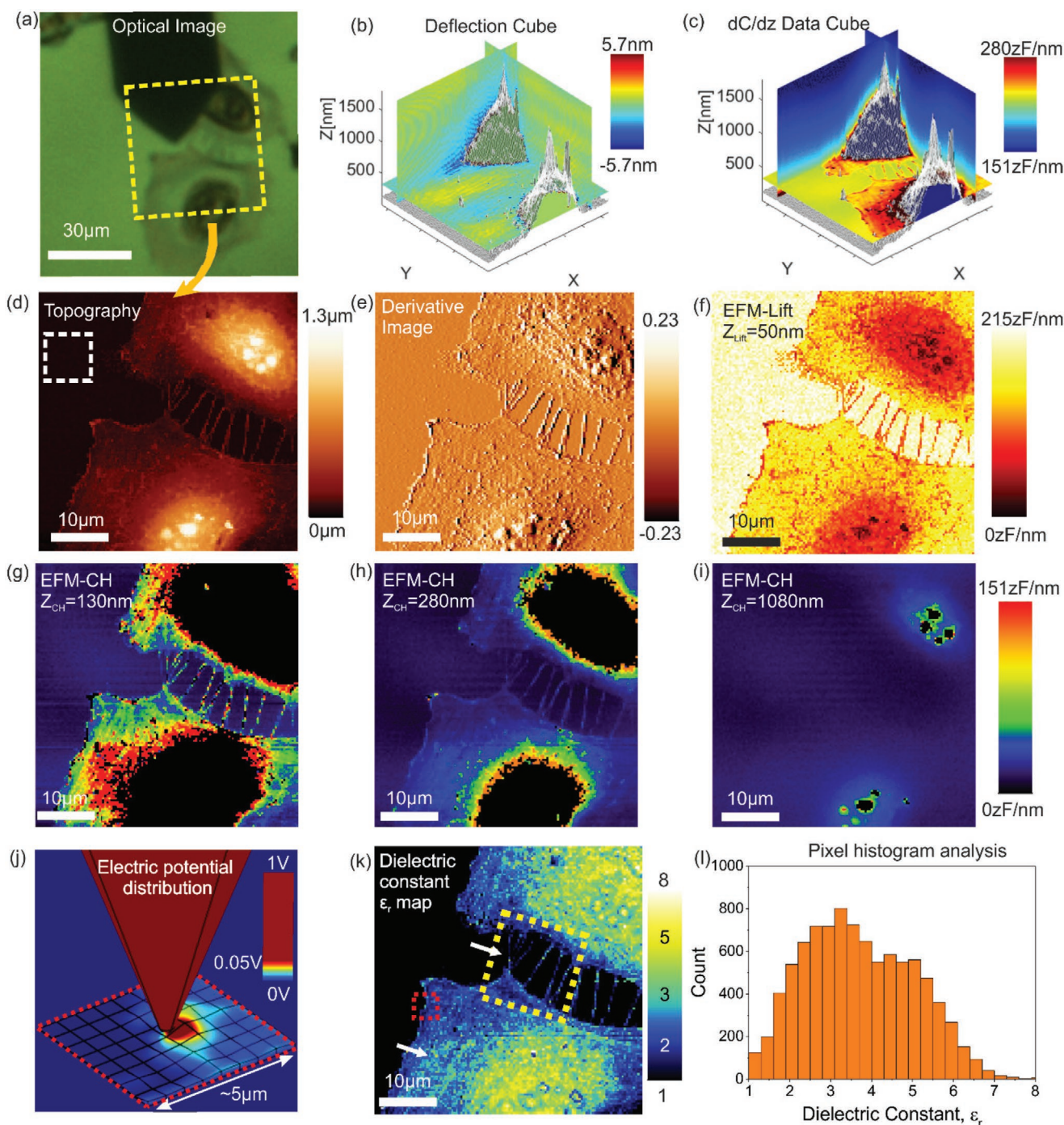
Figure 2. a) Optical image of two HeLa cells with the probe scanning on top of them. The yellow rectangle highlights the region on which the SDFVM data have been acquired. b) and c) Deflection and capacitance gradient data cubes, respectively. The data cubes have been built from 128×128 deflection and 2ω-oscillation amplitude approach curves acquired in the 70×70 μm^2 area highlighted by the yellow square in a). d) Topographic image extracted from the Deflection cube in (b). The white dashed rectangle indicates the region of the bare substrate used for the tip radius calibration (see Supporting Information S2). e) Derivative of the topographic image in (d) to better highlight the edges of the different cell regions and nanostructures. f) dC/dz lift-mode image at a distance $Z_{Lift} = 50$ nm obtained from the dC/dz data cube in (c). g)-i) dC/dz constant height-mode images at distances $Z_{CH} = 130$ nm, 280 nm and 1080 nm, respectively. The capacitance gradient is plotted in relative values with respect to the substrate. j) 9×9 pixel local cell geometric model corresponding to the pixel centered at (24,50), and calculated electric potential overlaid on its surface for $\varepsilon_r = 2$. k) Local dielectric constant map corresponding to the HeLa cells. The region highlighted with a red dashed square is the region whose topography is reconstructed in (j). The yellow dashed square highlights the region imaged in Figures 3a. l) Pixel histogram of the dielectric constant values of the map in (k).
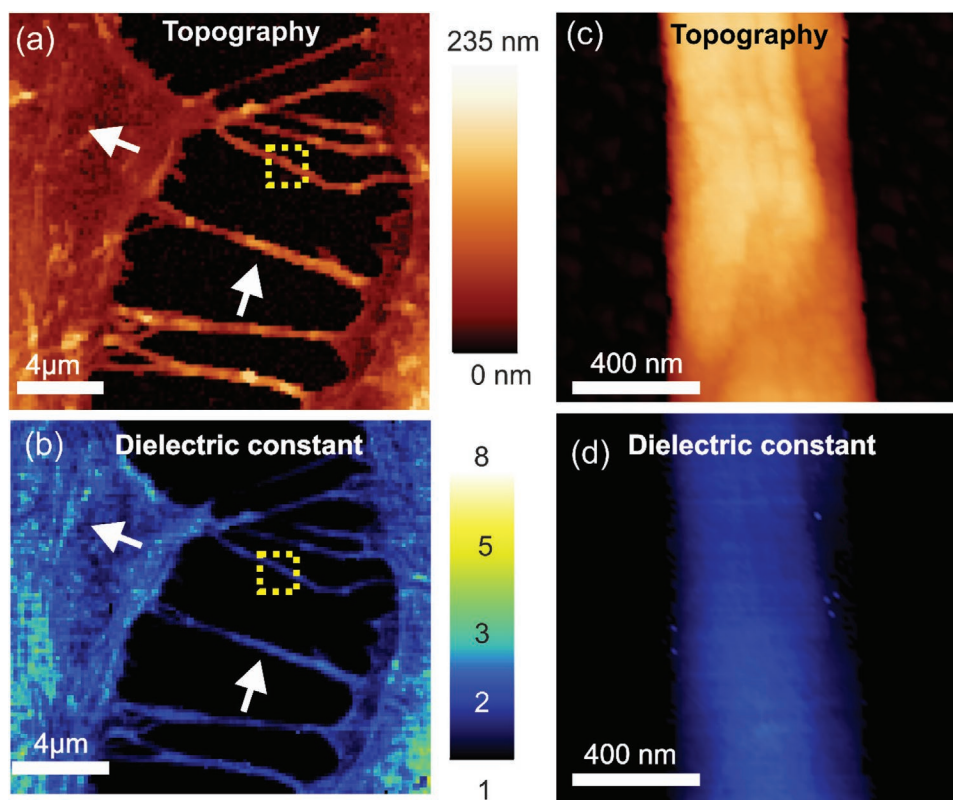
ADVANCED
SCIENCE NEWS
www.advancedsciencenews.com

small
methods
www.small-methods.com

Figure 3. a) Topographic image of the region in Figure 2d containing the cell membrane elongations joining the two HeLa cells. The image has been obtained from a set of SDFVM data acquired on the dashed yellow square region in Figure 2k. The arrows indicate the nanoelongations and the nano-filaments. b) Dielectric constant map of the region shown in (a) obtained after analyzing quantitatively the SDFVM data. Experimental parameters: 20×20 mm^2, 128×128 pixels. c) Topographic image of one of the nanoelongation joining the two HeLa cells obtained from a set of SDFVM data acquired on the dashed yellow square in Figure 3a. d) Dielectric constant map corresponding to (c) obtained after analyzing quantitatively the corresponding set of SDFVM data. Experimental parameters: 1.5×1.5 mm^2, 96×96 pixels.

rich in lipids. In fact, the dielectric constant value obtained for this region ($\varepsilon_1 \approx 2$) is remarkably close to the value corresponding to pure dry lipids, $\varepsilon_{lip} \approx 2$.[30,37] Moreover, the cell region with intermediate dielectric constant values ($\varepsilon_2 \approx 3$–4) is located in between the extended cell membrane region and the nucleus and has a thickness in the hundreds of nanometers range. This region corresponds to the cytoplasmatic region, which is especially rich in proteins. Again, the dielectric constant value measured $\varepsilon_2 \approx 3$–4 is within the range of values reported for dry proteins, $\varepsilon_{prot} \approx 3$–4.[22,37] Finally, the cell region with high dielectric constant values ($\varepsilon_3 \approx 5$–6) corresponds to the nucleus of the cell, which is rich in nucleic acids and proteins. Precisely, the dielectric constant obtained in this region represents well the value of a mixture of dry nucleic acids ($\varepsilon_{DNA} \approx 8$[21,16]) and proteins ($\varepsilon_{prot} \approx 3$–4[22,37]). These results show that, on the large scale, the dielectric constant map derived by means of SDFVM reflects the local biochemical composition of eukaryotic cells, in a similar way as it happened for the case of prokaryotic cells.[19]

More interestingly, we can also investigate the biochemical composition of small-scale nanostructures present in the eukaryotic cells. In Figure 2k, we identified two of such nanostructures, namely, nanoelongations joining the two cells and nanofilaments present in the cell body (both highlighted by arrows in Figure 2k). To analyze the biochemical composition of these nanostructures, we have acquired higher spatial

resolution SDFVM data in the region highlighted with the large yellow dashed square in Figure 2k. **Figure 3**a shows the topographic image of the region analyzed. In it, we can identify even more clearly both the cell membrane nanoelongations and the nanofilaments (both highlighted again by arrows). The nanoelongations are ≈500 nm wide, ≈200 nm high and several micrometers long. The nanofilaments are also micrometers long, and show a small diameter, difficult to determine in a precise way from the image since they are buried below the surface of the cell, but surely below a hundred of nanometers.

Figure 3b shows the corresponding dielectric constant map obtained by means of finite element numerical calculations (see the Supporting Information S4 for additional data). The dielectric constant map is quantitatively consistent with the map obtained for the larger scale image in Figure 2k, showing the quantitative reproducibility of the methodology used. The nanoelongations show a dielectric constant $\varepsilon_1 \approx 2$, what would imply a lipidic composition, while the nanofilaments show $\varepsilon_2 \approx 3$–4, what would imply a proteinic composition. No pixels with dielectric constant values larger than $\varepsilon_2 \approx 3$–4 are observed, indicating that nucleic acids are not present in the region imaged, what is consistent with the fact that the nucleus has not been included in the zoomed-in region analyzed. We highlight that the nanofilaments are located below the cell membrane, reflecting the subsurface sensitivity of SDFVM, as it has been shown earlier in other systems.[16,21,38]

Figure 3c shows a further zoom-in topographic image of one of the cell membrane nanoelongations obtained from a set of SDFVM data acquired in the yellow dashed square region in Figure 3a. The detailed topographic image reveals that the nanoelongations have a nonuniform height and width, with values varying in the ranges ≈100–200 and ≈400–700 nm, respectively. Despite these topographic variations, the dielectric constant map obtained (Figure 3d) is very uniform, with a value $\varepsilon_1 \approx 2$, confirming the result obtained from the larger scale image (Figure 3b), and, hence, confirming the lipidic composition of the nanoelongations.

As we have mentioned before, the main drawback of the approach used until here (and developed in Ref. [19]) is the very long computation times required to simulate by means of finite element numerical calculations the theoretical dC/dz approach curves at each pixel using realistic geometrical models and to extract the dielectric constant map by fitting them to the experimental SDFVM data. For a single pixel, this time is relatively short (≈1 h), but it can become very long (≈weeks or months) when all the pixels in the image are considered. In the case of whole eukaryotic cells, images contain at least 128 × 128 pixels, so that the number of pixels to be analyzed is $N_{pixels} > 10^4$, from where the very long times required for the analysis. To overcome this limitation, we propose here to use supervised neural networks (NN) to perform the analysis, in line with earlier proposals to study the dielectric properties of thin films from electrostatic force microscopy measurements[39,40,41,42] and with the current trend of exploiting the big data analysis in functional scanning probe microscopy studies.[43,44] Here, we use a built-in NN from the Scikit-learn python library.[45] The input data consist of three values of the capacitance gradient at three distances from the sample surface (dC/dz$_1$, dC/dz$_2$, dC/dz$_2$), the local volume below the tip (defined on a 4 × 4 pixel region around the pixel of interest), and the local roughness (defined as the standard deviation of the heights in the same 4 × 4 pixel region). Further details are given in the Experimental Section and in the Supporting Information S5. Like any other supervised learning algorithm, the NN needs to be trained with some previously labeled data. To perform the training, we used the dielectric constant values computed by using finite element numerical calculations for a small fraction of the total number of pixels. The accuracy of the predictions of the NN depends on the number of pixels used to train the network, as expected. **Figure 4** analyses the accuracy of the model predictions as a function of the percentage of data used in the training. Figure 4a,d,g shows the pixels randomly selected to train the NN in the case of 1%, 5%, and 10% training set sizes, respectively. Figure 4b,e,h shows the corresponding full dielectric constant maps calculated by the
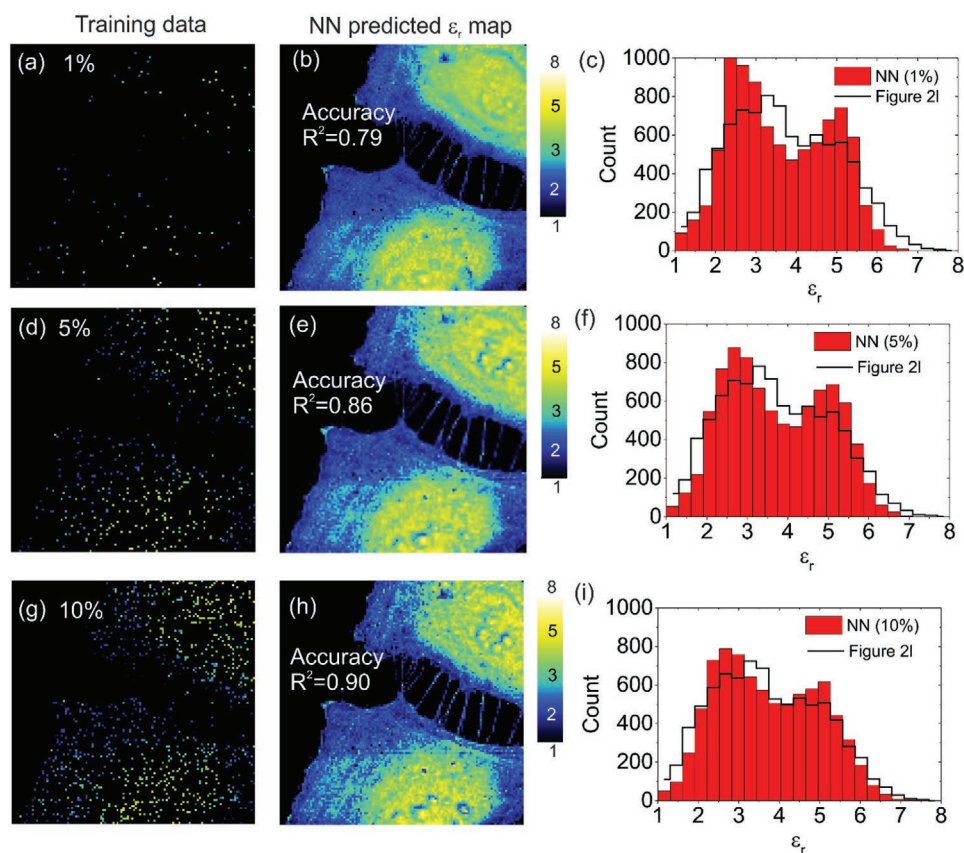

Figure 4. a) Dielectric constant map containing 1% of the pixels of Figure 2k used to train the NN. b) Dielectric constant map predicted by the NN trained with the pixels in (a). The predicted image has an accuracy $R^2 = 0.79$. c) Histogram of the NN predicted dielectric constant values in (b). The continuous line represents the histogram corresponding to the dielectric constant values calculated by means of finite element numerical calculations. The pixels used in the NN training are not included in the histogram. d)-f) and g)-i) same as (a)–(c) but for 5% and 10% of the pixels of Figure 2k used to train the NN, respectively. In this case the prediction accuracies in (e) and (h) are $R^2 = 0.86$ and 0.90, respectively.
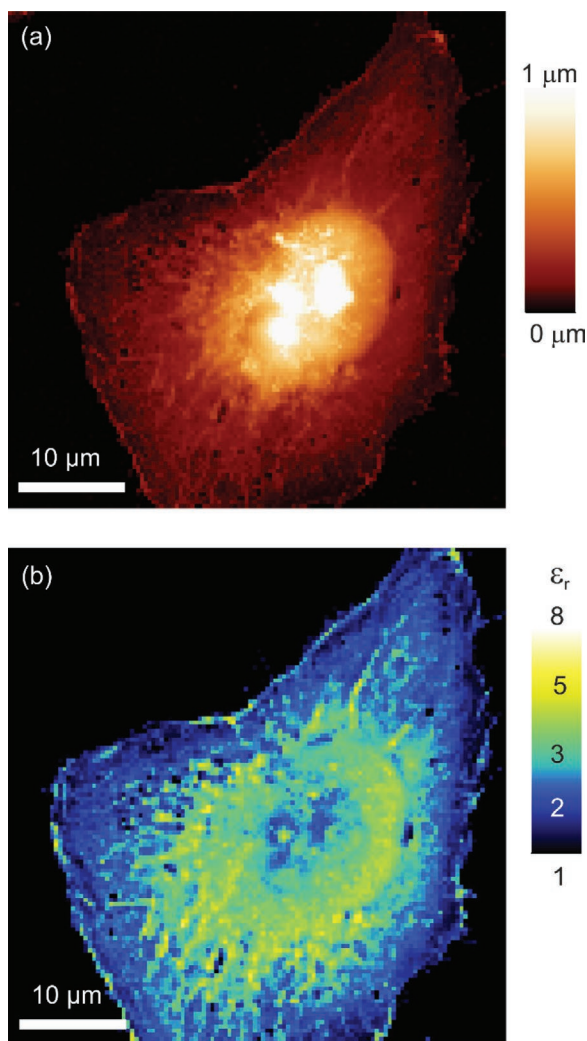
**ADVANCED
SCIENCE NEWS**
www.advancedsciencenews.com

**small
methods**
www.small-methods.com

Figure 5. a) Topographic image of a fixed HeLa cells on a gold-coated silicon substrate different from those in Figure 2 used to train the NN. The measurements have been done with the same probe. b) Corresponding dielectric constant map obtained by using the already trained NN. The calculation of this image is almost instantaneous. Experimental parameters: same as in Figure 2.

NN. Finally, Figure 4c,f,i shows the histogram representation of the dielectric constant values predicted by the NN in each case (red bars) and compare them with the histogram of the data obtained from the finite element numerical calculations (black line). As expected, when the number of pixels used to train the network is larger, the accuracy in the predicted dielectric constant map by the NN increases. We highlight that by only considering a 1% of the pixels to train the NN, the predicted dielectric constant map already shows a high accuracy ($R^2 = 0.79$) and presents the main features of the dielectric constant map calculated by means of finite element numerical calculations (compare Figures 4b with 2k). The accuracy of the predictions of the NN as a function of the size of the training dataset saturates quickly to $R^2 \approx 0.90$ with only $\approx$10% of the data used in the training. This means that in practice, the time to calculate the dielectric constant map of a given eukaryotic cell can be

reduced to just a 1–10% of the time required to compute it by using finite element numerical calculations.

More importantly, once sufficiently trained, the NN can be used to produce almost instantaneously dielectric constant maps corresponding to other cells with similar morphologies measured with the same probe. We illustrate it in **Figure 5**, where Figure 5a shows the topographic image of a HeLa cell different from the one used to train the NN. Figure 5b shows the dielectric constant map predicted by the trained NN applied to the corresponding SDFVM measurements performed on the cell.

The dielectric constant maps predicted by the trained NN (Figure 5b) shows similar features to the image fully calculated by means of finite element numerical calculations (Figure 2k), supporting the use of NN to generate fast dielectric constant maps of eukaryotic cells by using trained NN. Since the dielectric constant image is similar, the conclusions regarding the local biochemical composition of the cell are also similar. These results not only show the reliability of using supervised learning to produce accurate dielectric constant maps of eukaryotic cells from SDFVM measurements, but also open the door for in situ and on-the-fly label free nanoscale dielectric constant imaging via machine learning, as it unblocks the main bottleneck of the technique, namely, its complex, nonautomated, and time-consuming quantification process based on finite element numerical calculations (Figure 1).

3. Discussion

We have derived high spatial resolution local dielectric constant maps of fixed dry HeLa cells by means of SDFVM. From the dielectric constant maps, local biochemical composition information of the cells has been obtained in a label-free way, by matching up the measured dielectric constants to the known values of the dielectric constants of the main cell components in dry conditions ($\varepsilon_{lip} \approx 2$ for lipids,[30,37] $\varepsilon_{prot} \approx 3$–4 for proteins,[22,37] and $\varepsilon_{DNA} \approx 8$ for nucleic acids[16,21]).

Due to the long-range nature of the electric forces, the local dielectric constant values obtained by means of this approach, and hence the biochemical composition information, reflects the dominant component present in a nanometric small volume probed by the tip (see **Figure 6**). The size of the volume probed by the tip depends on the tip radius and half cone angle, the dielectric constants of the components contained in it and the thickness and local shape of the cell at the given position, so that it is difficult to estimate it, in general. As reference, we can use the estimation made for planar thick dielectric films,[36] where it was shown that the major contribution to the electric force ($\approx$50%) came from a volume of radius of the order of the tip radius $\approx$R. The high locality of the measurement is due to the sharp geometry of the tip, which makes the electric field intensity to be much higher below the tip apex than at distant regions. For the same reason, also a high lateral spatial resolution can be achieved, as we showed with the detection of the protein nanofilaments present in the cell body or the imaging of the cell membrane nanoelongations.

The actual lateral spatial resolution achievable in the dielectric constant maps is difficult to predict theoretically since it
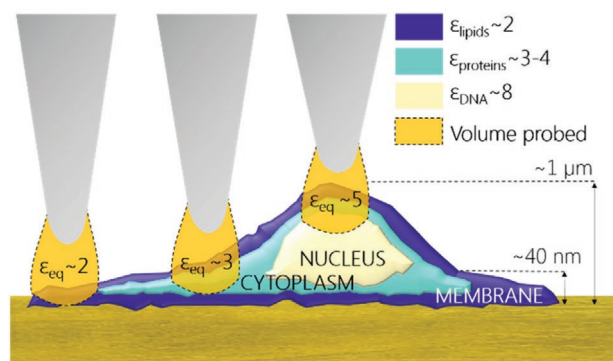
Figure 6. Schematic representation of the volume probed by the tip in SDFVM measurements on the different cell regions. The relation between the extracted local dielectric constant and the dielectric constants of the different cell components in the volume probed by the tip is highlighted in the three main cell regions, corresponding to the cell membrane, cytoplasm and nucleus.

depends on several factors including the actual cell topography and dielectric heterogeneity. In the large-scale images (e.g., $70 \times 70 \ \mu m^2$) the spatial resolution is limited by the pixel size, specially for images with relatively low number of pixels (e.g., 128×128 pixels). In this case, the pixel size is in the range of hundreds of nanometers (≈ 500 nm for a $70 \times 70 \ \mu m^2$ image with 128×128 pixels). For smaller scale images, the pixel size is not the limiting factor anymore, even at low pixel resolutions (≈ 16 nm for a $1.5 \times 1.5 \ \mu m^2$ image with 96×96 pixels). In this latter case, the spatial resolution is expected to be limited mostly by the tip radius and half cone angle, although to determine it in a precise way would require of a specific theoretical analysis.

From the technical side, some comments are needed. We emphasize that to obtain realistic dielectric constant maps useful for biochemical composition mapping, realistic cell geometries need to be considered in the derivation of the dielectric constant values. If this is not done (e.g., by resorting to simpler cell models valid for planar thin films as done in earlier works[25,26]) less realistic dielectric constant values are obtained, as we showed in the Supporting Information S3 and S6. This fact has been highlighted in previous works devoted to the dielectric characterization of nanoscale objects, such as nanoparticles,[16] bacterial cells,[17,18,19] bacterial endospores,[20] virus particles,[16] or protein macromolecular structures like virus tails[21] or bacterial flagella.[22] We also highlight that the use of full experimental and theoretical electric force approach curves at each pixel, instead of just one or few values obtained from electric force images acquired at different heights, largely improves the accuracy and reliability of the extracted local dielectric constant values. The use of full curves provides a more robust approach less prone to artefacts. Concerning environmental conditions, the relative humidity (RH) is one of the parameters that must be controlled during the measurements, since moisture is known to highly alter the dielectric measurements on biological samples, due to the high dielectric constant of water, $\varepsilon_{water} \approx 80$. This fact has been shown explicitly, for instance, for the case of dielectric measurements on bacterial cells[17] and bacterial endospores.[20] Environmental humidity effects are usually relevant when the relative humidity is RH > 40%.[17] The experiments

of the present work were done in a room with low humidity RH $\approx$ 30% controlled by an air conditioner, so the effects of moisture are expected to be neglectable in the results reported. In this respect, since the measurements are done under low humidity conditions, the composition identification is done by using the dielectric constant values of pure components measured in dry conditions.

The effect of the fixation agent on the measured local dielectric constants of the cells can also be an element of some concern. Based on the results reported here, its effects seem to be neglectable, since the values obtained for the dielectric constants measured in the cells can be consistently interpreted in terms of the values corresponding to pure components obtained without the use of any fixation agent. Here, we have used glutaraldehyde which is a crosslinking fixative that causes the deformation of proteins α-helices inducing mechanical hardening of the cells and preserving, as much as, possible the cell structure and composition.

Finally, we comment on the dielectric constant values obtained on isolated nanostructures, like the cell membrane nanoelongation in Figure 3c. For these nanostructures the relevance of tip convolution and finite size effects should be analyzed, as discussed elsewhere.[46,47] The nanoelongations have heights in the range $\approx$100–200 nm, and widths in the range $\approx$500–700 nm. For these dimensions, finite size effects can be relevant,[46] and hence the dielectric constant value extracted can depend on the actual size of the nanostructure, as we demonstrated for the case of nanoparticles and virus particles,[47] bacterial cells,[17,18,20] square slab thin films[46] and bacterial flagella.[19] While the height of the nanostructure can be accurately determined from the topographic image, its width is affected by tip convolution effects, which tend to increase it. For this reason, the geometrical model used to extract the dielectric constant is, in general, wider than the actual geometry of the nanostructure. This fact can produce dielectric constant values systematically lower than the actual values.[47] However, applying tip-convolution analysis to nanostructures with nonregular geometries, like the cell membrane nanoelongations, is very complex, and in general, it cannot be done in an unambiguous way. The fact that the nanoelongations show an almost uniform dielectric constant value ($\varepsilon_1 \approx 2 \pm 0.4$) despite its relatively irregular shape and size constitutes an indication that finite size and tip convolution effects are probably not very relevant in the present case.

There is still some room for improvement in the nanoscale dielectric and composition mapping of eukaryotic cells by SDFVM. Tip convolution effects could be minimized by using either sharper tips (although the signal will be also reduced) or applying a tip-deconvolution filter to the topographic image (although tip deconvolution is not always a well posed inverse problem for irregular geometries). The spatial resolution could be reduced by using also sharper tips, but also by considering more complex cell dielectric theoretical models to account for the lateral and vertical spatial variability of the dielectric constants in the volume probed by the tip. This would require assigning different dielectric constants to each voxel of the local geometric model and to use advanced tomographic reconstruction algorithms, not available yet, despite the progress made recently.[48]

**ADVANCED
SCIENCE NEWS**
www.advancedsciencenews.com

**small
methods**
www.small-methods.com

The dielectric and composition mapping could be in principle extended to fixed cells in water environment and to living cells. Scanning dielectric microscopy has been already demonstrated in the water environment,[49,50,51] and it has been applied to probe the dielectric properties of systems like supported lipid bilayers,[52,53] self-assembled monolayers (SAMs),[54] and electrolyte gated field effect transistors.[55] The presence of water can make ionic conductivity effects relevant what imposes the realization of the measurements at frequencies above the relaxation frequency of the water solution, usually in the 10's MHz range, to prevent ionic screening effects.[49,50,51] The use of high frequencies requires of specific measuring set-ups and methods, as detailed elsewhere.[49,54] The presence of water introduces also a medium of high polarizability ($\varepsilon_{water} \approx 80$) in the volume probed by the tip. Therefore, the local equivalent homogeneous dielectric constant of the cell, ε_{eq}, will reflect both the local composition of the cell and the water content of the volume probed. This effect should be included in the modeling and taken into account in the interpretation of the dielectric constant maps obtained. In addition, the presence of water can make the dielectric constant values of reference for the pure components to vary with respect to those in dry conditions. At present, dielectric constant values of reference in fully hydrated conditions measured by SDM are only available for lipids[52] and lipid/cholesterol mixtures.[53] The presence of water can introduce also a softening of the cells even if fixed. This fact can make more difficult to determine the "true" topography of the cells, specially when imaged with probes adequate for SDM measurements, thus complicating the quantitative analysis and the derivation of the dielectric constant maps. Finally, fully hydrated cells, even if fixed, can be considerably taller than dried cells (roughly a factor three to five taller), reaching heights in the range 5–10 μm in the nuclear regions and some hundreds of nanometers in the cell extended parts. Since, electrostatic forces decrease with tip substrate distance, a much lower sensitivity to the dielectric properties is expected on the highest parts of the cell for this reason.

Extending the measurements to living cells, involves additional challenges with respect to those found in performing the measurements on fixed cells in water solutions. Living cells are, first, mobile, so that fast imaging will be a prerequisite. The time required to acquire the experimental SDFVM data could be improved by using high resonance frequency cantilevers (like the ones developed for high-speed AFM), as discussed elsewhere.[19] Currently, the speed at which the ac electric force curves are acquired is limited by the frequency of the ac electric voltage applied, which in turn is limited by the mechanical resonance frequency of the cantilever (since the electrical frequency is set in the flat zone of the mechanical spectrum of the cantilever to avoid spurious mechanical contribution to the acquired signal). Considering higher resonance frequency cantilevers could allow increasing the speed of the acquired force curves and hence reduce the experimental acquisition times.[19] In addition, ionic conductivity effects in living cell imaging can become much more relevant. Physiological buffer solutions have usually high ionic strengths (at least 100×10^{-3} м), what would imply the realization of the SDM measuremts in the range of 100's MHz frequencies, making the set-up adaptations more delicate and exigent. Furthermore, the conductivity of the extracellular solution can be smaller than the conductivity of the intracellular medium, what can make the dielectric response frequency dependent, what has to be taken into account in the modeling. Finally, the issue related to the soft nature of the cells is much more relevant in the case of living cells, since nonfixed cells present a Young's modulus orders of magnitude smaller than that of fixed cells.[56]

Regarding the dielectric maps quantified by means of supervised learning, the accuracy of the presented machine learning methodology ($R^2 = 0.90$) has also some room for improvement. Both the NN architecture (number of hidden layers, activation function, convolutional/nonconvolutional structure) and the input feature selection can be further optimized by performing a deeper analysis, which lies beyond the scope of the present work. The procedure presented here still requires the use of finite element numerical calculations to derive the labeled dataset to train the neural network. We have shown that, once trained, the neural network can predict the dielectric constant map of cells imaged with the same probes if the cells show similar features to the ones of the image used to train the neural network. We envision that by using labeled training datasets obtained in a large number of cells and with different probes, it should be possible to train a neural network that will be able to predict accurately the dielectric constant maps of a wide range of cells irrespectively of the probe used and with no further training required. In this case, there would be no need of finite element numerical calculations at all. The prospects for the implementation of the machine learning strategy presented in this work to a scanning probe microscopy controller system are exciting. A well trained NN would make on-the-fly in- situ label-free nanoscale dielectric constant imaging a reality regardless the complexity of the system under study, what extends the interest of this perspective to other research fields, but specially to material science, where the study of dielectric properties of complex systems is of great interest.

4. Conclusion

We have shown that quantitative nanoscale dielectric constant maps of dry eukaryotic cells that reflect their local biochemical composition can be obtained in a label-free way by means of scanning dielectric microscopy measurements in force volume detection mode. We have validated the methodology by recovering well known facts, such as the lipidic nature of the cell membrane, the protein rich nature of the cytoplasm region, and the nucleic acid rich nature of the nucleus. In addition, we have shown the full potential of the method by analyzing the dielectric properties and biochemical composition of nanostructures present in the cell, such as cell membrane nanoelongations and nanofilaments present in the cell body close to its surface. A striking boost in the time needed to obtain the dielectric constant maps is found when the labor-intensive finite element numerical quantification methods are substituted by modern and easy-to-use supervised machine learning algorithms, preserving a great accuracy in the dielectric constant resolution. These results open interesting applications in Cell and Molecular Biology, as well as, in fields such as Material Science, Nanotoxicity, or Drug Delivery.

**ADVANCED
SCIENCE NEWS**

www.advancedsciencenews.com

**small
methods**

www.small-methods.com

5. Experimental Section

HeLa Cell Growth and Sample Preparation: HeLa cells from a lab cell line were used in the present study. The protocol to prepare the sample was optimized from the different options shown elsewhere.[57] The cells were seeded at 50 k cells mL^{-1} onto gold coated silicon substrates (Arrandee) placed in a petri dish with Dulbecco's modified eagle medium (DMEM, as received with L-Glutamine, 4.5 g L^{-1} D-glucose and pyruvate, Gibco) supplemented with FBS 10% (Gibco) and penicillin/streptomycin 1% (Biowest). After 24 h of incubation in 5% CO_2 and 37 °C, the cells were observed and seemed completely attached and spread on the gold substrate. Then, cells were fixed. The medium was washed with PBS, and the cells were incubated with 2.5% glutaraldehyde in PBS for 10 min. After fixation, the cells were rinsed with PBS and then dried. The cells were washed consecutively with different solutions: 75%, 50%, and 25% PBS and ultrapure MiliQ water, and 25%, 50%, 75%, 85%, 95%, and 100% ethanol for 5 min each. Finally, the cells were immersed for 5 min in Hexamethyldisilazane and let dry in the desiccator before imaging.

Scanning Dielectric Force Volume Microscopy Measurements: SDFVM measurements were carried out by following the method described earlier,[19] which was based on previous developments of the SDM technique.[16,29–32] In a nutshell, an ac electric voltage of frequency ω was applied between the conductive probe of an AFM system and the conductive substrate. The applied potential induces a static bending of the cantilever and its oscillation at double of the excitation frequency. The static deflection and the 2ω-oscillation amplitude were recorded with a Nanowizard 4 AFM system (JPK) mounted on a T-1 Eclipse optical microscope (Nikon) and connected to an external lock-in amplifier (eLockin 204/2, Anfatec). The data acquisition was carried by using the Advanced Quantitative Imaging mode (JPK) in ambient conditions at room temperature and environmental humidity ≈30% RH controlled by a room air conditioner. Each set of SDFVM data consisted of 128 × 128 deflection and 2ω-oscillation amplitude approach curves, each one with 900 data points and spanning a length of 1800 nm. The acquisition time per pixel was 200 ms, and the lock-in integration time was set to 1 ms, with a gain Glock-in = 200. The ac applied voltage amplitude was $v_{ac} = 3$ V and the frequency of the applied voltage $f_{el} = 4$ kHz, much smaller than half the resonance frequency of the cantilevers ($f_0 = 19$ kHz). We used diamond coated conductive probes (CDT-CONTR) with nominal equivalent spring constants in the range $k = 0.5$ N m^{-1}(nominal), which was calibrated with the thermal noise method giving $k = 0.72$ N m^{-1}. Raw deflection and 2ω-oscillation amplitude approach curves were converted into calibrated deflection and capacitance gradient data as detailed earlier[16] by using the relationships

$$D(nm) = \frac{D_{RAW}(V)}{m(V/nm)} \quad (1)$$

$$\frac{dC}{dz}(aF\,nm^{-1}) = \frac{4k(nN\,nm^{-1})\left(A_{2\omega}(V) - A_{2\omega,offset}(V)\right)}{v_{AC}(V)^2\,m\left(\frac{V}{nm}\right)G_{lockin}} \quad (2)$$

Here, m is the photodiode sensitivity (i.e., the slope of the contact part of the vertical deflection approach curve), k is the equivalent spring constant, and $A_{2\omega,offset}$ the lock-in offset. The photodiode sensitivity, m, was taken as the average value of the values obtained on a bare part of the substrate (see the Supporting Information S7). The noise of the measurements in the present conditions was ≈2 zF nm^{-1}. The SDFVM data cubes and topographic and electric images were obtained as explained in detail elsewhere.[19]

Finite Element Numerically Calculated Dielectric Constant Maps: The quantification of the SDFVM data sets to derive the local equivalent homogeneous dielectric constant images was done by following the methods of SDM[16,29–32] implemented for force volume data as detailed in.[19] In a nutshell, finite element numerical calculations, using realistic sample and tip models were used to calculate capacitance gradient dC/dz approach curves at each pixel of the image. The capacitance gradient

values, dC/dz, were calculated from the electric force acting on the tip ($F_{2\omega} = 1/4$ dC/dz v_0^2) obtained by solving the Poisson's equation for the tip-sample system and integrating the Maxwell stress tensor over the tip surface. The theoretical dC/dz approach curves were fitted to the experimental ones at each pixel with the equivalent homogeneous dielectric constant as single fitting parameter. The dielectric constant value obtained is assigned to the given pixel, generating the so called dielectric constant map (see Supporting Information S8 for the full analysis of one pixel). To avoid too long computational times, the sample geometry does not include the full cell, but only a grid of nxn pixels around the calculated pixel, where n is adjusted for each specific image, depending on the pixel size, to guarantee that the region effectively probed by the tip is included in the modelling. For Figure 2k we took n = 9 (which corresponds to an area 5 × 5 µm^2), for Figure 3b we also took n = 9 (which in this case corresponds to an area of 1.7 × 1.7 µm^2) and for Figure 3d we took n = 41 (which corresponds to an area of 0.65 × 0.65 µm^2). With these choices, and the appropriate meshing conditions (see Supporting Information S9), we ensured that the geometric effects on the local polarization of the sample were correctly accounted for. Note that a set of local sample geometries equal to the number of pixels analyzed need to be built. An example of how local computations were made is illustrated in Supporting Information Video S2. The tip geometry was modeled as usual in SDM[16,31,32,36] as a cone with a tangent sphere and caped with a disc cantilever at the top. The tip radius, R, and half cone angle, θ, were calibrated from approach curves taken on a bare part of the metallic substrate, as detailed elsewhere.[16,31,32,36] The microscopic tip parameters were set to their nominal values in the calibration procedure: cone height H = 12.5 µm, cantilever thickness W = 3 µm, disc cantilever radius H·tan(θ)+L, with L = 3 µm. Calculations and fittings were done by using COMSOL Multiphysics 5.3a linked to a custom software code written in MATLAB (MathWorks).

Neural Network Calculated Dielectric Constant Maps: The supervised learning approach implemented in this work to calculated the dielectric constant maps uses a built in Multi-layer Perceptron (MPL) regressor from the scikit-learn python library.[45] The MPL is fed with six input features per sample (pixel) in its input layer, which pretend to account for all the needed information to reconstruct the hidden function that correlates SDFVM data with local dielectric constants. The input features are the images of the experimentally measured dC/dz for three different tip-sample distances (dC/dz$_1$, dC/dz$_2$, dC/dz$_3$), the topography image, the volume under the tip image, and the local surface roughness image (see Supporting Information S5). The input features are normalized using a scaling function, which removes the mean and scales the data to unit variance. The solver uses a stochastic gradient-based optimizer to train the NN. The choice of input features has some room for improvement if feature selection algorithms are considered and cleverer input features are tested, but as the NN maps obtained here were precise enough with this choice, we did not consider it for the present work. The main hyperparameters of the MPL are the following: one hidden layer consisting of 100 neurons and a rectified linear unit function (f(x) = max(0,x)) as activation function. There is also room for improvement in terms of finding the optimal structure of the NN hyperparameters to further increase the model accuracy (which saturates to around $R^2 \approx 0.90$ in the present case), but we consider it out of the scope of the present work. Finally, the output layer consists only of 1 neuron which is the dielectric constant of the pixel itself.

The procedure to obtain the machine learning calculated dielectric constant maps is the following. First, the MPL is trained with labeled samples (pixels whose local dielectric constant had been calculated with the realistic finite element numerical calculations). Once the network is trained, new unlabeled samples (pixels where the local dielectric constant is unknown) are input to the network and its output consist of the local dielectric constant of that pixel. By repeating the procedure for all the pixels of the image, full dielectric constant images from the MPL regressor outputs can be obtained. The training of the NN can be carried by considering a small fraction of the pixels of the image (1-10% depending on the accuracy required). Once the NN is properly trained it can be applied directly to other cells not used in its training. The time

consumption of this approach is remarkably better than that based on the use of finite element numerical calculations, as full dielectric constant maps can be calculated in seconds, improving by several orders of magnitude the aforementioned state-of-the art quantification process which needed normally several weeks to calculate large scale images.

Supporting Information

Supporting Information is available from the Wiley Online Library or from the author.

Acknowledgements

Conflict of Interest

The authors declare no conflict of interest.

Data Availability Statement

Data available on request from the authors.

Keywords

[1] K. Thorn, *Mol. Biol. Cell.* **2016**, *27*, 219.
[2] S. Pujals, N. Feiner-Gracia, P. Delcanale, I. Voets, L. Albertazzi, *Nat. Rev. Chem.* **2019**, *3*, 68.
[3] S. J. Sahl, S. W. Hell, S. Jakobs, *Nat. Rev. Mol. Cell Biol.* **2017**, *18*, 685.
[4] E. A. Specht, E. Braselmann, A. E. Palmer, *Annu. Rev. Physiol.* **2017**, *79*, 93.
[5] V. Marx, *Nat. Methods* **2019**, *16*, 1209.
[6] D. Evanko, *Nat. Methods* **2010**, *7*, 36.
[7] S. Kretschmer, M. Pieper, G. Hüttmann, T. Bölke, B. Wollenberg, L. M Marsh, H. Garn, P. König, *Lab. Invest.* **2016**, *96*, 918.
[8] P. Friedl, K. Wolf, U. H von Andrian, G. Harms, *Curr. Protoc. Cell Biol.* **2007**, *34*, 4.15.1.
[9] H. Lee, K. Kang, K. Mochizuki, C. Lee, K.-A. Toh, S. A. Lee, K. Fujita, D. Kim, *Nano Lett.* **2020**, *20*, 8951.
[10] T. Guerenne-Del Ben, Z. Rajaofara, V. Couderc, . V. Sol, H. Kano, P. Leproux, J.-M. Petit, *Sci. Rep.* **2019**, *9*, 13862.
[11] V. Astratov, *Label-Free Super-Resolution Microscopy*, Springer, Berlin **2019**.
[12] Y. Cotte, F. Toy, P. Jourdain, N. Pavillon, D. Boss, P. Magistretti, P. Marquet, C. Depeursinge, *Nat. Photonics* **2013**, *7*, 113.
[13] K. Asami, *Colloid. Polym. Sci.* **1995**, *273*, 1095.
[14] M. Schwarz, M. Jendrusch, I. Constantinou, *Electrophoresis* **2020**, *41*, 65.
[15] R. Pethig, *Dielectrophoresis: Theory, Methodology and Biological Applications, Chichister*, John Wiley & Sons, New York **2017**, Ch. 8.
[16] L. Fumagalli, D. Esteban-Ferrer, J. L. Carrascosa, G. Gomila, *Nat. Mater.* **2012**, *11*, 808.
[17] D. Esteban-Ferrer, M. A. Edwards, L. Fumgalli, A. Juárez, G. Gomila, *ACS Nano* **2014**, *10*, 9843.
[18] M. C. Biagi, R. Fabregas, G. Gramse, M. Van Der Hofstadt, A. Juárez, F. Kienberger, L. Fumagalli, G. Gomila, *ACS Nano* **2015**, *10*, 280.
[19] M. Checa, R. Millan-Solsona, N. Blanco, E. Torrents, R. Fabregas, G. Gomila, *Nanoscale* **2019**, *11*, 20809.
[20] M. Van Der Hofstadt, R. Fabregas, R. Millan-Solsona, A. Juarez, L. Fumgalli, G. Gomila, *ACS Nano* **2016**, *10*, 11327.
[21] A. Cuervo, P. D. Dans, J. L. Carrascosa, M. Orozco, G. Gomila, L. Fumagalli, *Proc. Natl. Acad. Sci. USA* **2014**, *111*, E3624.
[22] H. Lozano, R. Fabregas, N. Blanco-Cabra, R. Millán-Solsona, E. Torrents, L. Fumagalli, G. Gomila, *Nanoscale* **2018**, *10*, 19188.
[23] S.-S. Tuca, G. Badino, G. Gramse, E. Brinciotti, M. Kasper, Y. J. Oh, R. Zhu, C. Rankl, P. Hinterdorfer, F. Kienberger, *Nanotechnology* **2016**, *27*, 135702.
[24] M. Farina, J. C. Hwang, A. Di Donato, E. Pavoni, G. Fabi, A. Morini, F. Piacenza, E. Di Filippo, T. Pietrangelo, *IEEE/MTT-S Int. Microwave Symp.*, IEEE, Piscataway, NJ **2018**, p. 111.
[25] A. Valavade, K. Date, M. Press, D. Kothari, *Biomed. Phys. Eng. Express* **2018**, *4*, 055023.
[26] A. Valavade, D. Kothari, C. Löbbe, *AIP Conf. Proc.* **2013**, *1512*, 520.
[27] W. Zhao, W. Cui, S. Xu, L. Z. Cheong, D. Wanga, C. Shen, *Nanoscale Adv.* **2019**, *1*, 537.
[28] W. Zhao, L.-Z. Cheong, W. Cui, S. Xu, C. Shen, *J. Microsc.* **2019**, *275*, 75.
[29] L. Fumagalli, G. Ferrari, M. Sampietro, G. Gomila, *Appl. Phys. Lett.* **2007**, *91*, 243110.
[30] L. Fumagalli, G. Ferrari, M. Sampietro, G. Gomila, *Nano Lett.* **2009**, *9*, 1604.
[31] L. Fumagalli, G. Gramse, D. Esteban-Ferrer, M. A. Edwards, G. Gomila, *Appl. Phys. Lett.* **2010**, *96*,183107.
[32] L. Fumagalli, G. Gomila, in *Capacitance Spectroscipy of Semiconductors*, Jenny Standford Publishing, Singapore **2018**, Ch. 13.
[33] Y. F. Dufrêne, D. Martínez-Martín, I. Medalsy, D. Alsteens, D. Müller, *Nat. Methods* **2013**, *10*, 847.
[34] L. F. Jiménez-García, R. Fragoso-Soriano, *J. Struct. Biol.* **2000**, *129*, 218.
[35] M. Van der Hofstadt, R. Fabregas, M. Biagi, L. Fumagalli, G. Gomila, *Nanotechnology* **2016**, *27*, 405706.
[36] G. Gramse, G. Gomila, L. Fumagalli, *Nanotechnology* **2012**, *23*, 205703.
[37] A. Dols-Perez, G. Gramse, A. Calò, G. Gomila, L. Fumagalli, *Nanoscale* **2015**, *7*, 18327.
[38] L. Fumagalli, A. Esfandiar, R. Fabregas, S. Hu, P. Ares, A. Janardanan, Q. Yang, B. Radha, T. Taniguchi, K. Watanabe, G. Gomila, K. S. Novoselov, A. K. Geim, *Science* **2018**, *360*, 1339.
[39] G. M. Sacha, F. B. Rodríguez, P. Varona, *Nanotechnology* **2009**, *20*, 085702.
[40] E. Castellano-Hernández, F. B. Rodríguez, E. Serrano, P. Varona, G. M. Sacha, *Nanoscale Res. Lett.* **2012**, *7*, 250.
[41] E. Castellano-Hernández, G. M. Sacha, *Appl. Phys. Lett.* **2012**, *100*, 023101.
[42] M. Konomi, G. M. Sacha, *Ultramicroscopy* **2017**, *182*, 243.

ADVANCED
SCIENCE NEWS

www.advancedsciencenews.com

small
methods

www.small-methods.com

[43] S. V. Kalinin, B. G. Sumptere, R. K. Archibald, *Nat. Mater.* **2015**, *14*, 973.

[44] X. Li, L. Collins, K. Miyazawa, T. Fukuma, S. Jesse, S. V. Kalinin, *Nat. Commun.* **2018**, *9*, 2428.

[45] F. Pedregosa, G. Varoquaux, A. Gramfort, V. Michel, B. Thirion, O. Grisel, M. Blondel, P. Prettenhofer, R. Weiss, V. Dubourg, J. Vanderplas, A. Passos, D. Cournapeau, M. Brucher, M. Perrot, *J. Mach. Learn. Res.* **2011**, *12*, 2825.

[46] G. Gomila, G. Gramse, L. Fumagalli, *Nanotechnology* **2014**, *25*, 255702.

[47] G. Gomila, D. Esteban-Ferrer, L. Fumagalli, *Nanotechnology* **2013**, *24*, 505713.

[48] R. Fabregas, G. Gomila, *J. Appl. Phys.* **2020**, *127*, 024301.

[49] G. Gramse, M. Edwards, L. Fumagalli, G. Gomila, *Appl. Phyis. Lett.* **2012**, *101*, 213108.

[50] M. Checa, R. Millan-Solsona, G. Gomila, *Phys. Rev. E* **2019**, *100*, 022604.

[51] G. Gramse, M. Edwards, L. Fumagalli, G. Gomila, *Nanotechnology* **2013**, *24*, 41709.

[52] G. Gramse, A. Dols-Perez, M. Edwards, L. Fumagalli, G. Gomila, *Biophys. J.* **2013**, *104*, 1257.

[53] M. Di Muzio, R. Millan-Solsona, J. H. Borrell, L. Fumagalli, G. Gomila, *Langmuir* **2020**, *36*, 12963.

[54] R. Millan-Solsona, M. Checa, L. Fumagalli, G. Gomila, *Nanoscale* **2020**, *12*, 20658.

[55] A. Kyndiah, M. Checa, F. Leonardi, R. Millan-Solsona, M. Di Muzio, S. Tanwar, L. Fumagalli, M. Mas-Torrent, G. Gomila, *Adv. Funct. Mater.* **2021**, *31*, 2008032.

[56] R. Garcia, *Chem. Soc. Rev.* **2020**, *49*, 5850.

[57] L. Francis, D. Gonzalez, T. Ryder, K. Baer, M. Rees, J. White, R. Conlan, C. Wright, *J. Microsc.* **2010**, *240*, 111.